

Numerical Heat Transfer, Part A: Applications

An International Journal of Computation and Methodology

ISSN: 1040-7782 (Print) 1521-0634 (Online) Journal homepage: <http://www.tandfonline.com/loi/unht20>

Molecular dynamics study of wettability and pitch effects on maximum critical heat flux in evaporation and pool boiling heat transfer

Ricardo Diaz & Zhixiong Guo

To cite this article: Ricardo Diaz & Zhixiong Guo (2017) Molecular dynamics study of wettability and pitch effects on maximum critical heat flux in evaporation and pool boiling heat transfer, Numerical Heat Transfer, Part A: Applications, 72:12, 891-903, DOI: [10.1080/10407782.2017.1412710](https://doi.org/10.1080/10407782.2017.1412710)

To link to this article: <https://doi.org/10.1080/10407782.2017.1412710>



Published online: 20 Dec 2017.



Submit your article to this journal [↗](#)



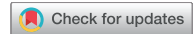
Article views: 25



View related articles [↗](#)



View Crossmark data [↗](#)



Molecular dynamics study of wettability and pitch effects on maximum critical heat flux in evaporation and pool boiling heat transfer

Ricardo Diaz and Zhixiong Guo 

Department of Mechanical and Aerospace Engineering, Rutgers, The State University of New Jersey, Piscataway, New Jersey, USA

ABSTRACT

Molecular dynamics simulations were employed to investigate the effects of wettability (contact angle) and pitch on nanoscale evaporation and pool boiling heat transfer of a liquid argon thin film on a horizontal copper substrate topped with cubic nano-pillars. The liquid–solid potential was incrementally altered to vary the contact angle between hydrophilic ($\sim 0^\circ$) and hydrophobic ($\sim 127^\circ$), and the pitch (distance between nano-pillars) was varied between 21.7 and 106.6 Å to observe the resultant effect on boiling heat transfer enhancement. For each contact angle, the superheat was gradually increased to initiate nucleate boiling and eventually pass the critical heat flux (CHF) into the film boiling regime. The CHF increases with pitch, and tends to decrease substantially with increasing contact angle. A maximum overall heat flux of $1.59 \times 10^8 \text{ W/m}^2$ occurs at the largest pitch investigated (106.6 Å), and as the contact angle increases the superheat required to reach the CHF condition also increases. Finally, in certain cases of small pitch and large contact angle, the liquid film was seen to transition to a Cassie–Baxter state, which greatly hindered heat transfer.

ARTICLE HISTORY

Received 13 September 2017
Accepted 14 November 2017

1. Introduction

Heat transfer on the micro- and nanoscales continues to be a vital area of research due to the ever-decreasing size of electro-mechanical components and devices and the accompanying increases in power density resulting from the rapid technological advances of the last decade [1–3]. As applications with large power densities increase, it will be extremely important to remove excess heat as efficiently as possible [4]. Boiling heat transfer on micro/nanoscale substrates, which has the capacity for rapid large heat flux removal, is an excellent candidate for such applications but requires further research to better understand the heat transfer process and mechanism at these small scales [5]. In particular, pool boiling heat transfer enhancement has long been investigated both experimentally and numerically as a means of meeting the high heat flux removal requirements. Various methods of enhancement, including the use of micro/nanostructures, nanofluids, and hydrophilic/phobic substrates, have been employed and their effects on heat transfer have been studied.

Recent advances in micro- and nanoscale fabrication techniques have allowed for better customization of substrates via micro/nano-channels, nanostructures, etc. These enhanced topologies passively increase boiling heat transfer via increased surface area and bubble nucleation sites [6–8].

CONTACT Zhixiong Guo  guo@jove.rutgers.edu  Department of Mechanical and Aerospace Engineering, Rutgers, The State University of New Jersey, Piscataway, NJ 08854, USA.

Color versions of one or more of the figures in the article can be found online at www.tandfonline.com/unht.

© 2017 Taylor & Francis

Nomenclature

| | |
|---|---|
| <p>c integer numerical constant (dimensionless)</p> <p>d system dimensionality (dimensionless)</p> <p>E potential energy (eV)</p> <p>f force vector of atom i (eV/Å)</p> <p>k_B Boltzmann constant (eV/K)</p> <p>N number of atoms (dimensionless)</p> <p>P pressure (bar)</p> <p>r interparticle distance (Å)</p> | <p>r_c cutoff radius for particle interaction calculations (Å)</p> <p>r_i position vector of atom i (Å)</p> <p>T temperature (K)</p> <p>V volume (Å³)</p> <p>Greek symbols</p> <p>ϵ Lennard–Jones potential well depth (eV)</p> <p>σ Lennard–Jones characteristic length (Å)</p> |
|---|---|

Wang et al. [9] showed that altered bubble dynamics due to micro/nanostructures could also improve critical heat flux (CHF). Cooke and Kandlikar [10] also showed that adding micro-channels to the substrate surface improves the heat transfer coefficient by promoting wetting of the surface and preventing dry out, while Mandel et al. [11] found increased heat transfer coefficients in thin films for reduced superheats and channel widths in microscale channels. Nanofluids have also been investigated in pool boiling, and shown to improve CHF via enhanced fluid conductivity, surface wetting, energy absorption, and nanoparticle deposition on the substrate, which increases surface roughness [12–15]. Micro-convection via Brownian motion and nanoparticle aggregation have also been postulated as CHF enhancement mechanisms in nanofluid pool boiling [16]. More recently, hydrophobic/philic patterning has been investigated experimentally [17, 18] and shown to increase bubble nucleation and CHF via increased wetting. Several of the above-mentioned pool boiling experiments have attained heat fluxes greater than 10 kW/cm², which is two orders of magnitude larger than traditional pool boiling.

The effect of liquid contact angle on evaporation and CHF has also been investigated in simulations [19] and experiments [20, 21], and others [22, 23] proposed correlations for pool boiling CHF that incorporated contact angle, among other variables. In general, these studies showed that CHF is adversely affected by large contact angles (hydrophobicity), while smaller (hydrophilic) contact angles increase the heat transfer coefficient and improve CHF. It is difficult, however, to perform these types of experiments on the nanoscale while controlling for a number of different variables. On such a small scale, larger bubble sizes (radii $\geq 1 \mu\text{m}$) are not allowed to form, and the dynamics and heat transfer mechanisms can be very different.

Thus, molecular dynamics (MD) simulations have been utilized in this study to investigate the effect of equilibrium contact angle on CHF in nanoscale evaporation and pool boiling. In the context of this work, CHF refers to the maximum heat flux to the thin liquid film achieved before the onset of explosive boiling/dry out. MD simulation is a powerful tool that can be used to investigate nanoscale phenomena with more flexible control than experimental setups [24]. In this study, the substrate topology (roughness), temperature, and pressure were all controlled to more clearly view the effect of contact angle on the CHF condition. To date, many MD studies have been conducted on both homogeneous and heterogeneous systems to investigate heat transfer, phase change, flow properties, etc. Several studies [25–27] have used flat substrates to investigate evaporation, effect of wettability, etc. and there have recently been some studies focused on boiling/evaporation on nanostructured substrates using differently shaped nanostructures and nanostructures with different wettability [28–31]. Nevertheless, to the authors' knowledge, no MD study has been conducted looking at maximum CHF with contact angle and pitch variations.

In this study, a nanostructured copper substrate is used to heat a liquid argon film. Several different scenarios were investigated, including eight different contact angles, ranging from hydrophilic to hydrophobic, and six different pitches. Simulation of these arrangements has allowed us to compare the CHF and evaporation characteristics of each to determine heat transfer trends, and investigate mechanisms by which the heat transfer enhancements take place.

2. Simulation method

The system used in the main simulations was comprised of a horizontal solid copper wall with vertically oriented nano-pillars, a layer of liquid argon, and argon vapor molecules in a simulation box with varying dimensions based on pitch, which are detailed in Table 1. Figure 1a–c details the overall configuration of a typical simulation and the enlarged views of the copper wall and nano-pillars, respectively. The wall at the bottom of the simulation box consisted of a base of five monolayers of solid copper. As in previous works, this was deemed enough to accurately act as a conduction layer for liquid heating [9, 28, 29, 32, 33]. The nano-pillars were arranged on the base wall in a symmetrical fashion. The nano-pillars were 15 monolayers high and each measured $25.3 \times 25.3 \times 25.3 \text{ \AA}$. The base wall and nano-pillars were arranged in an face centered cubic (FCC) lattice structure corresponding to the (100) plane. For these copper atoms, a lattice constant of 3.615 \AA was used, corresponding to a density of 8.9 g/cm^3 . In all, 15 monolayers of argon molecules were placed just above the copper base wall, covering both the wall and pillars. For the argon liquid atoms, a lattice constant of 5.256 \AA was used, corresponding to an initial density of 1.4 g/cm^3 . Finally, argon vapor atoms (corresponding to a density of $5.77 \times 10^{-3} \text{ g/cm}^3$) were placed above the liquid, filling the rest of the simulation box.

Interactions between all atoms were modeled with the standard 12–6 Lennard–Jones potential [34], given by:

$$E = 4\epsilon \left[\left(\frac{\sigma}{r} \right)^{12} - \left(\frac{\sigma}{r} \right)^6 \right], \text{ for } r < r_c \quad (1)$$

where ϵ is the potential well depth, σ is the characteristic length at which the potential becomes zero, r is the interatomic length, and r_c is the cutoff distance. The r^{-12} term governs short-range repulsion, whereas the r^{-6} term describes long-range attraction. To reduce the computational cost, an r_c equal to $4\sigma_{\text{Ar–Ar}}$ was employed. For interactions between two atoms i and j , it follows that

$$\sigma_{ij} = \frac{1}{2} (\sigma_i + \sigma_j) \text{ and } \epsilon_{ij} = \sqrt{\epsilon_i \epsilon_j} \quad (2)$$

Before the main CHF simulation runs, separate simulations were first carried out using altered interaction potential parameters to establish the different contact angles. The $\epsilon_{\text{Cu–Ar}}$ interaction value for the 106° contact angle (i.e., $\epsilon_{\text{Cu–Ar}} = 0.0653 \text{ eV}$) was calculated via the normal Lorentz–Berthelot mixing rules of Eq. (2); however, for most cases, the Cu–Ar potential well depth was altered to change the interaction strength, and consequently the contact angle. The altered potential well depth is calculated as follows:

$$\epsilon_{\text{Cu–Ar}} = c \cdot \sqrt{\epsilon_{\text{Cu}} \epsilon_{\text{Ar}}} \quad (3)$$

where c is a user-chosen numerical constant. Each case is meant to simulate a copper substrate with altered wetting characteristics (via surface modification, coatings, etc.). Table 2 details the potential parameters and the resulting contact angles of 0° , 57° , 76° , 92° , 103° , 116° , 121° , and 127° . A smaller ϵ value indicates a weaker, or more hydrophobic, interaction (i.e., a larger contact angle). For clarity, each case will be referred to with a CA followed by its contact angle value, that is, CA-0, CA-57, etc.

Table 1. Simulation domain parameters based on pitch (¼ model).

| Pitch (Å) | Dimensions (Å) | # Cu atoms | # Ar atoms |
|-----------|---------------------------------|------------|------------|
| 21.7 | $47.0 \times 47.0 \times 440$ | 3160 | 2135 |
| 27.1 | $52.4 \times 52.4 \times 440$ | 3790 | 2588 |
| 45.2 | $70.5 \times 70.5 \times 440$ | 5273 | 5442 |
| 65.1 | $90.4 \times 90.4 \times 440$ | 7720 | 9424 |
| 85.0 | $110.3 \times 110.3 \times 440$ | 10,990 | 13,757 |
| 106.6 | $131.9 \times 131.9 \times 440$ | 15,010 | 20,777 |

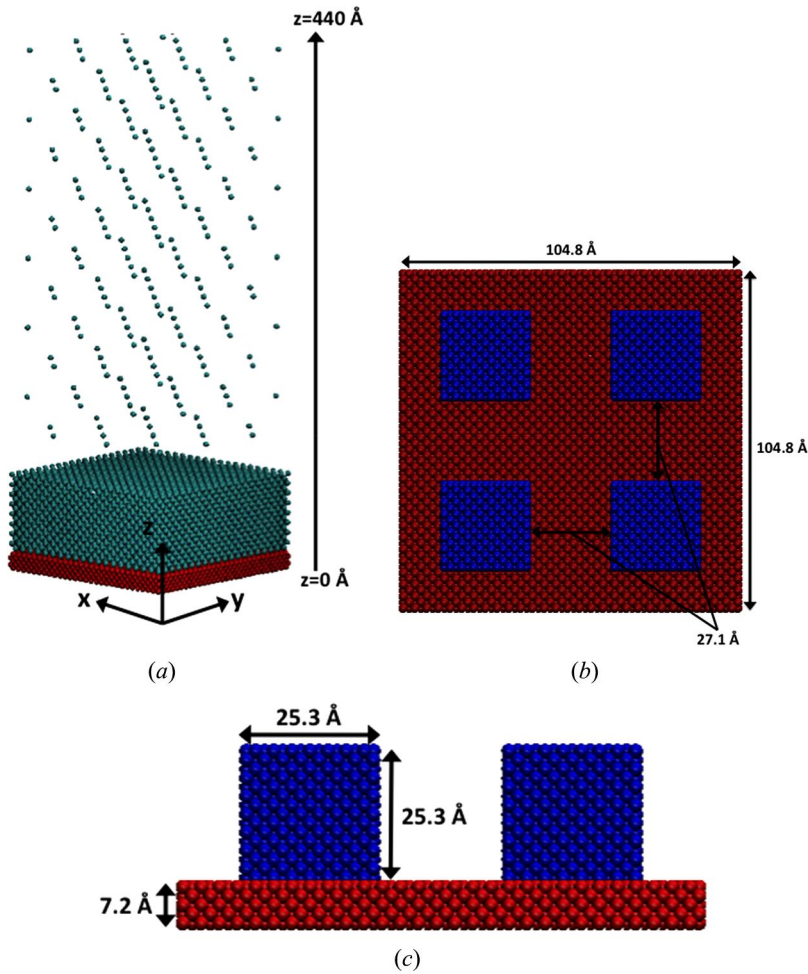


Figure 1. Sketch of the 27.1 Å pitch simulation model: (a) overall simulation configuration (1/4 was considered in computation due to symmetry), (b) and (c) enlarged views of the copper substrate and nano-pillars.

The separate contact angle simulations were performed on a flat copper substrate with the same dimensions as the substrate used in the CHF simulations. A block of liquid argon particles was initially placed just above the substrate while argon vapor atoms filled the rest of the simulation box. The liquid block runs the entire length (in the y -direction) of the simulation box, resulting in a cylindrical “infinite length” droplet. From previous work [35], this is shown to better approximate the macro-contact angle in nanoscale studies. The simulation was run for 3.5 ns with a 5 fs time step, whereas a Langevin

Table 2. Potential well-depth parameters and resultant contact angles.

| Case | f | $\epsilon_{\text{Cu-Arg}}$ (eV) | Contact angle ($^\circ$) |
|--------|------|---------------------------------|----------------------------|
| CA-0 | 0.09 | 0.0059 | 0 |
| CA-57 | 0.08 | 0.0052 | 57 |
| CA-76 | 0.07 | 0.0046 | 76 |
| CA-92 | 0.06 | 0.0039 | 92 |
| CA-103 | 0.05 | 0.0033 | 103 |
| CA-116 | 0.04 | 0.0026 | 116 |
| CA-121 | 0.03 | 0.0020 | 121 |
| CA-127 | 0.02 | 0.0013 | 127 |

thermostat was applied to keep all atoms at 90 K. To simulate the resulting contact angle, the simulation domain was first divided into a grid of boxes $\sim 2 \text{ \AA}$ per side, and the average density was monitored in each and written to a file every 250 ps. The last four data points were then averaged to determine the final density profile, an example of which is shown in Figure 2. As in [35], a small portion of the liquid region near the wall was excluded to remove any influence of the copper wall on the contact angle calculation. Once the profile was calculated, an algebraic circle fit was used to estimate the droplet boundary as well as its intersection with the horizontal substrate. With the circle and intersection point defined, a contact angle could be calculated.

After the contact angles were established, the CHF simulations were carried out in two phases. Phase I consisted of initialization and equilibration, and was itself broken down into three sub-phases. First, an energy minimization was carried out to determine the minimum energy state of the initial configuration. Once completed, a Langevin thermostat was imposed on all atoms to establish an equilibration temperature of 90 K. After 3 ns, the thermostat was removed, and the system was allowed to evolve under the microcanonical ensemble (NVE) for an additional 1 ns. Once the system temperature and energy are stable, Phase II commences and the temperature of the system is steadily increased from 90 to 300 K over the course of 7.5 ns (not including the previous 4 ns of Phase I), to move fully through the explosive boiling regime and show the full CHF curve. In this phase, the Langevin thermostat was applied to only the second monolayer of the copper base wall, whereas the first (bottom) layer was kept immobile to prevent atoms from moving through the bottom of the simulation domain. The upper three levels of the copper atoms were maintained in the NVE ensemble and allowed to interact as they normally would via the Lennard–Jones potential. Both phases used a velocity Verlet integration algorithm with a 5 fs time step.

The simulation domain is periodic in the four sidewalls of both the x - and y -directions, which helps to prevent finite size effects of the small simulation domain. To reduce the computational time required, 1/4 of the arrangement shown in Figure 1 (i.e., only one nano-pillar) was used for the simulations. The results from the smaller domain were compared to the four nano-pillar domains and showed no significant differences in pressure, temperature, density, or heat flux. The CPU time required was reduced by 42%, with the larger domain requiring 32.1 h and the smaller domain only requiring 13.6 h. The top of the simulation domain is a fixed, adiabatic boundary, which means that any atom that moves outside the boundary by a certain distance is placed back inside the boundary by that same distance, while having the sign of its z velocity reversed. All simulations were run using LAMMPS software (version 16 Feb 2016), a classical molecular dynamics code based on Plimpton's work [36], while system visualization was performed with VMD v1.9.1 [37]. All simulations were performed on a workstation cluster of 75 2.6 GHz Intel Sandy Bridge 2670 CPUs, with typical runs requiring 6.7–21.8 h of run time (depending on pitch) and 4–9 MB of memory per processor.

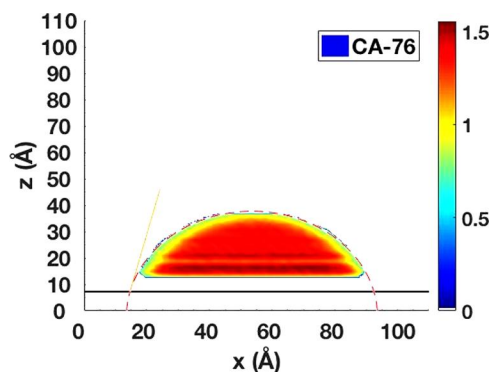


Figure 2. Density map of the CA-76 simulation.

3. Results and discussion

During Phase I equilibration, the average pressure in the z -direction was monitored to determine system stability. Pressure was calculated via the following formula:

$$P = \frac{Nk_B T}{V} + \frac{\sum_{i=1}^N r_i \cdot f_i}{dV} \quad (4)$$

where N is the number of atoms, T is the temperature, V is the domain volume, d is the system dimensionality (in this case 3), and r_i and f_i are the position and force vectors of atom i , respectively. The equilibration is meant to take place at atmospheric pressure conditions, while during Phase II the pressure is allowed to evolve as it normally would in a closed system. Figure 3 shows the z component of the pressure in the vapor region (i.e., $z > 75 \text{ \AA}$) for both Phases I and II of the 27.1 \AA pitch case. As can be seen, most cases maintain a vapor pressure of about 1 bar during the 4 ns of Phase I before showing a relatively steady pressure increase during Phase II. The vapor pressures recorded are in line with those seen in previous experimental works [38]. CA-0 through CA-116 are grouped together until roughly 6 ns, when separation starts to occur. In general, the more hydrophilic (lower contact angle) cases exhibit higher vapor pressures as the temperature rises, which suggests increased evaporation. This holds true for all pitches considered in this study.

Figure 4a and b shows the temperature history for copper and argon, respectively. As expected, the copper temperature is virtually the same for all cases, and after the equilibration at 90 K it rises linearly to 300 K over the duration of the simulation. The argon temperature initially follows a similar path due to the slow nature of the temperature increase, however soon after Phase II begins all cases tend to follow the copper temperature less closely (there is a 10–60 K lag between the copper and argon temperatures). Again, some separation between the different cases emerges, with the more hydrophilic cases showing a higher temperature. Between 7 and 8 ns, the rate of temperature increase for most cases then begins to slow down. This is due to the onset of the CHF condition and subsequent vapor layer formation for the various cases, as will be seen in later figures. After this point, in certain cases, there is a temperature rate increase that corresponds to the full vaporization of the liquid slug, which is ejected from the substrate during the onset of explosive boiling. These general trends hold true for larger pitches as well although the CHF onset tends to occur at higher temperatures. At the 27.1 \AA pitch shown in the figure, the CA-121 and CA-127 cases are once again anomalous, and there is no clear region where the rates of temperature increase change. This is most likely

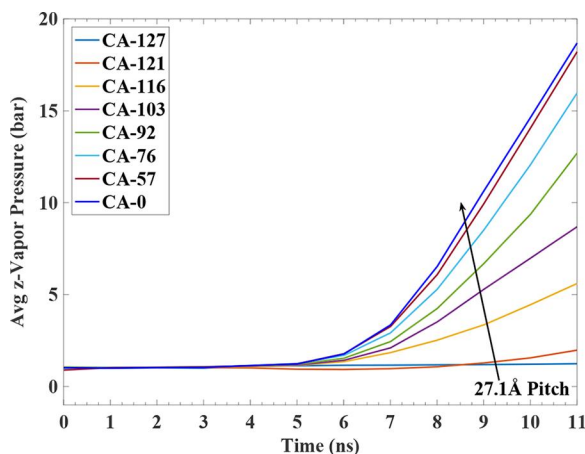


Figure 3. Argon z -vapor pressure evolution.

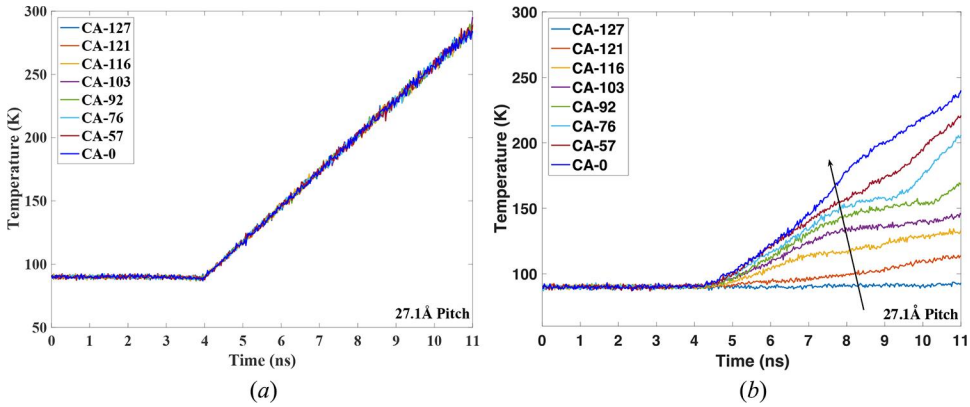


Figure 4. Temperature history for (a) copper and (b) argon.

due to the CHF condition not being reached for these cases, though for larger pitches this is not always the case.

Figures 5 and 6 show the density during Phase II and the evaporation ratio for both phases, respectively. To calculate the density, the simulation domain was divided into boxes encompassing the entire x - and y -directions and 7.9 \AA in the z -direction, and the average density in each box was recorded every 10 ps . The density measurements for all cases were restricted to the liquid region

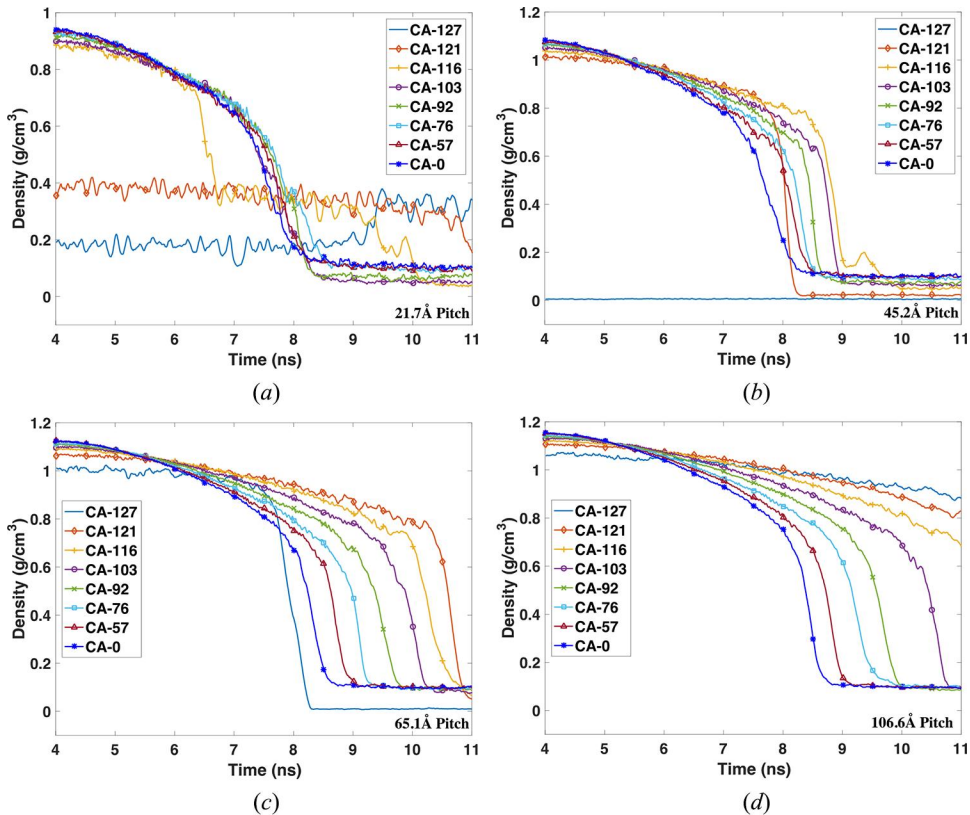


Figure 5. Phase II density profiles for (a) 21.7 \AA pitch, (b) 45.2 \AA pitch, (c) 65.1 \AA pitch, and (d) 106.6 \AA pitch.

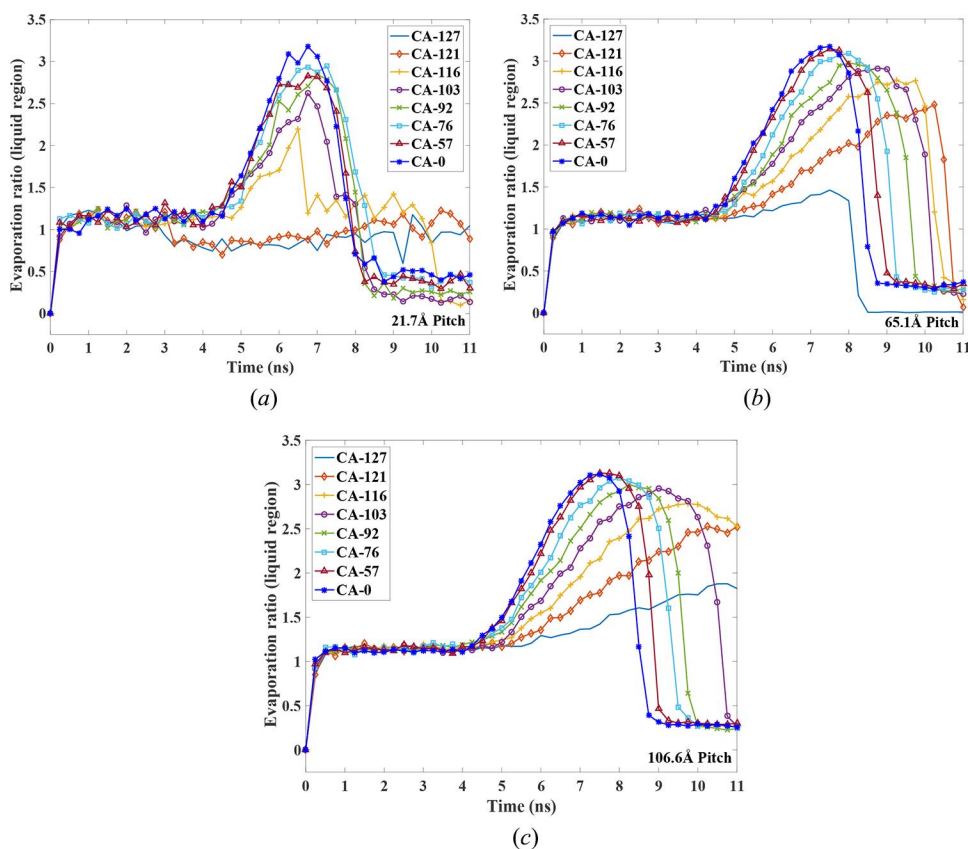


Figure 6. Evaporation ratio (in the liquid region, $z < 50 \text{ \AA}$): (a) 21.7 \AA pitch, (b) 65.1 \AA pitch, and (c) 106.6 \AA pitch.

(i.e., less than or equal to 50 \AA). The density values at the end of Phase I/beginning of Phase II ($\sim 1\text{--}1.2 \text{ g/cm}^3$) show good agreement with the thermodynamic properties of argon liquid for the given pressure and temperature. From the very beginning of Phase II separation is apparent, with stronger interaction potentials (i.e., lower contact angles) predictably resulting in higher densities. The separation decreases as each case nears its CHF point (marked by a sharp drop in density), with all but the three most hydrophobic cases in the 21.7 \AA pitch scenario (Figure 5a) having a density near 0.7 g/cm^3 at 7 ns. CA-116 shows an earlier density drop due to the brief onset of a Cassie–Baxter condition, while the CA-121 and CA-127 cases begin Phase II already in the Cassie–Baxter state due to having weaker potential interactions. For comparison, Figure 5b–d shows the 45.2 , 65.1 , and 106.6 \AA pitch scenarios, respectively. In general, as the pitch increases the temperature at which CHF occurs also increases, as does the density difference between contact angles. The CA-121 and/or the CA-127 cases remain anomalous until the 106.6 \AA pitch case, where there is a clear trend in the onset of CHF, which increases in time as hydrophobicity increases. This makes sense, as better heat transfer (and thus earlier onset of CHF) is expected from the more hydrophilic cases. The density curves begin as slowly decreasing, and then move to a region of faster exponential decrease as the CHF is approached before transitioning to a nearly constant density after the CHF. In a macro-sense, this exponential density decrease is due to the sharp increase in nucleation rate that accompanies the CHF condition [39]. While the small-scale nature of these simulations makes it difficult to directly observe bubble nucleation, the rate of phase change from liquid to vapor can be viewed via the evaporation ratio, in Figure 6. This shows the ratio of the evaporation number at a certain time to the initial number of vapor atoms within the liquid region. To distinguish between liquid and vapor

atoms, a criterion based on coordination number [31] was used, where any argon atom surrounded by less than 12 other atoms (within a radius of 5.3 \AA) is considered a vapor atom. In this way, the number of liquid and vapor atoms can be tracked and compared between cases. For the 21.7 \AA pitch case shown in Figure 6a, within the liquid there is indeed a spike in the number of evaporated argon atoms coinciding with the CHF near 7 ns. The CA-0 case has the largest ratio, which suggests better heat transfer; however, it should be noted that there is not a direct (one-to-one) correlation between evaporation and CHF, and it will later be seen that the evaporation ratio peaks are more closely spaced than the heat flux peaks. In the 65.1 \AA pitch case of Figure 6b, the peaks occur later in the simulation, and the evaporation ratio is increasing with decreasing contact angle. This trend continues in Figure 6c (106.6 \AA pitch case), and due to a lack of any anomalous Cassie–Baxter states each peak occurs at increasing times (and superheats) as the contact angle is increased. Of the contact angles and pitches considered, the 106.6 \AA pitch is the only case that exhibits no Cassie–Baxter transition.

The CHF curves for the 21.7 , 65.1 , and 106.6 \AA pitches are shown in Figure 7a–c. To calculate heat flux, the total energy (kinetic and potential) of the argon atoms was tracked each time step, then divided by the time step size and surface area of the substrate to calculate the heat flux. The fluxes for all the present cases are in line with previous simulations [40], as well as the heat flux limit predicted by the evaporative kinetic theory [41]. Interestingly, at smaller pitches, both the CHF and the temperature at which the peak flux occurs tend to increase with increasing contact angle up to a point, after which the CHF begins to decrease. For the 21.7 \AA pitch scenario (Figure 7a), CA-0 shows the maximum CHF ($\sim 1.01 \times 10^8 \text{ W/m}^2$), which is 6.3 times the minimum case of CA-127

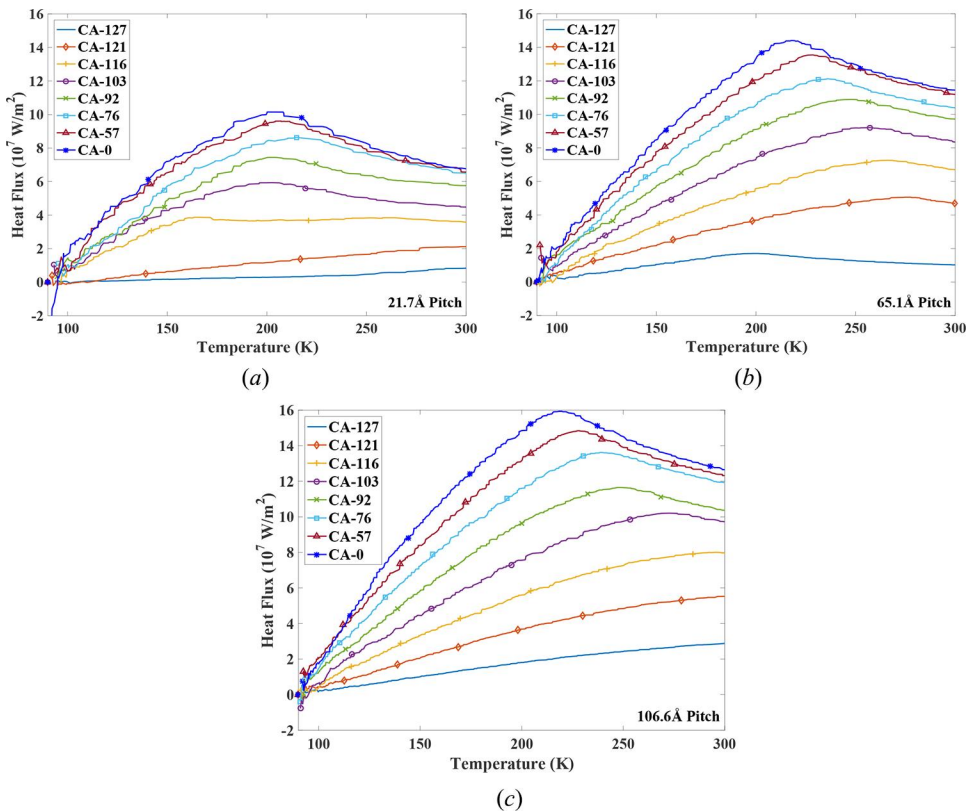


Figure 7. CHF curves (argon heat flux vs. Copper temperature) for (a) 21.7 \AA pitch, (b) 65.1 \AA pitch, and (c) 106.6 \AA pitch. Note: CHF, critical heat flux.

($\sim 0.16 \times 10^8 \text{ W/m}^2$) and a 5.3% increase over CA-57 ($\sim 0.96 \times 10^8 \text{ W/m}^2$). For most cases, the temperature required to reach the CHF condition is grouped relatively closely near 200 K although the CA-116, CA-121, and CA-127 cases are not due to the Cassie–Baxter transition. Indeed, here it is confirmed that CA-121 and CA-127 do not reach CHF at all, as their fluxes are seen to slowly increase through the entirety of the simulation time.

In the 65.1 Å pitch scenario (Figure 7b), CA-0 case shows a higher overall CHF ($\sim 1.44 \times 10^8 \text{ W/m}^2$) than the lower pitch cases, and is 8.4 times CA-127 ($\sim 0.171 \times 10^8 \text{ W/m}^2$) and a 6.7% over CA-57 ($\sim 1.35 \times 10^8 \text{ W/m}^2$). At this pitch, the peaks are less concentrated, with CA-0's peak (at 229 K) $\sim 12 \text{ K}$ lower than CA-57, and $\sim 60 \text{ K}$ lower than CA-121. Here, all cases reach CHF although CA-127 remains anomalous with a peak at 200 K, which is much earlier than the other cases.

The overall trend shows that as the pitch is increased the more hydrophilic cases tend to improve CHF performance as compared to the more hydrophobic cases, and the maximum CHF shifts toward greater superheats. This trend continues for the 106.6 Å pitch case (Figure 7c), where CA-0 shows the highest flux ($\sim 1.59 \times 10^8 \text{ W/m}^2$, at 220 K). This is 5.5 times higher than CA-127 ($\sim 0.29 \times 10^8 \text{ W/m}^2$), and $\sim 7\%$ higher than CA-57. CA-127 once again does not reach CHF; however, in this case, it is due to the superheat required exceeding 300 K rather than effects of Cassie–Baxter state. Overall, this largest pitch scenario looks most like what would be expected from a macro-scale study, where increasing hydrophilicity corresponds to greater heat transfer and earlier onset of CHF.

Figure 8a shows the plot of the peak CHF as a function of contact angle. As can be seen, the most hydrophilic case shows the highest peak flux at all pitches, and there is a non-linear decrease in flux with increasing contact angle. This decrease is due to the weakening interaction between liquid and substrate, no longer allowing efficient kinetic energy exchange. This trend is in line with previous experimental and theoretical studies [19, 22, 42] in which more hydrophilic substrates produced higher flux values. Also, the 85.0 and 106.6 Å pitches have extremely close flux profiles; thus, it would be reasonable to assume that increasing the pitch further would do very little to increase the maximum heat flux.

Figure 8b shows the increase in peak heat flux with increasing pitch. Once again it can be seen that the peak flux increases with increasing pitch, non-linearly. The 106.6 Å pitch case has a 57% increase in CHF over the 21.7 Å case, a $\sim 10\%$ increase over the 65.1 Å case, and only a $\sim 1\%$ increase over the 85.0 Å case. This suggests that the peak flux eventually reaches a peak value somewhere slightly above a 106.6 Å pitch. In previous larger-scale studies [18, 43], smaller pitches corresponded with higher heat flux, which suggests that after the peak the flux values will start to decrease rather than plateau; however, more simulations are needed to confirm.

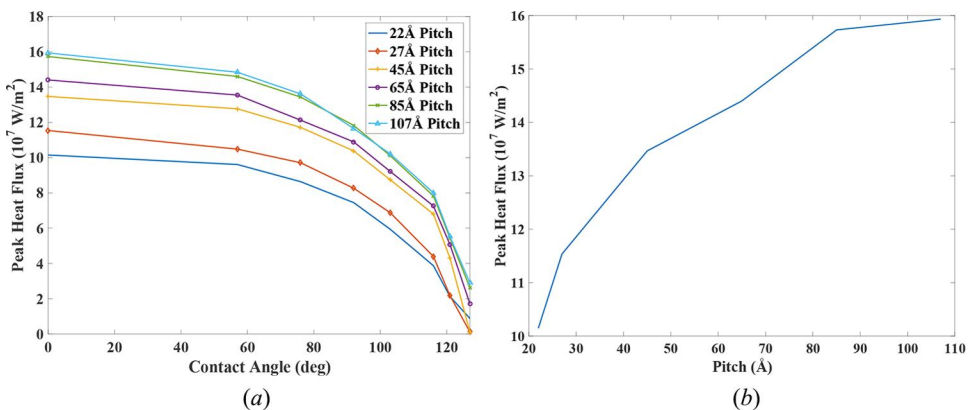


Figure 8. Peak heat flux curves: (a) peak flux vs. Contact angle and (b) maximum CHF vs. Pitch. Note: CHF, critical heat flux.

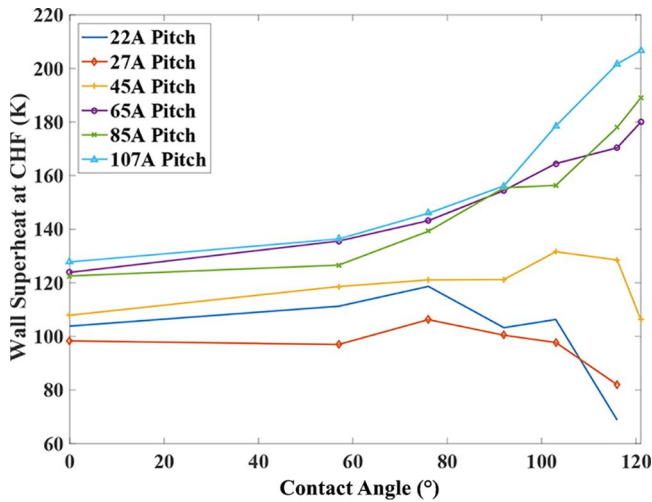


Figure 9. Wall superheat at CHF vs. Contact angle. *Note:* CHF, critical heat flux.

Figure 9 shows the wall superheat at the CHF condition vs. contact angle for each pitch scenario. Two distinct groups can be seen in this plot, with the three smallest pitches in one group and the three largest in the other. For the three largest pitches, the superheat required to attain CHF increases with both increasing contact angle and pitch, which is expected. Increased wettability at low contact angles aids in kinetic energy transfer, leading to faster onset of the CHF condition. At higher contact angles, heating of the liquid occurs more slowly (per Figure 4) due to reduced liquid–solid particle interaction, leading to additional superheating before the CHF condition is met. The lowest three pitches begin similarly to the previous group, with an increase (albeit slight) in superheat with increasing contact angle. This initial rise, however, is followed by an eventual drop in required superheat. The combination of low pitch and hydrophobic interaction results in the Cassie–Baxter transition, which alters the dynamics of the system. These low superheats could be due to the pitch being of similar length to the critical bubble radius (in this case ~ 20 Å). Instead of a bubble nucleating, growing, and then finally separating from the substrate (as in a high pitch case), a growth-hindered bubble would be less likely to separate, eventually coalescing with nearby bubbles to form a vapor layer near the substrate and leading to the CHF condition. Regarding pitch, although the lower pitch scenarios (namely the 21.7 and 27.1 Å cases) have lower overall heat fluxes, they also reach CHF at much lower wall superheats, which could be desirable in applications that need to remain at lower temperatures for mechanical or efficiency reasons.

4. Conclusion

Evaporation and film boiling of a thin liquid argon film on a nanostructured copper substrate was investigated via MD simulation. After obtaining CHF curves based on varying contact angles and pitches, and monitoring temperature, density, pressure, and evaporation, the following observations were made:

- In line with previous studies, it was found that for a given pitch, there is an inverse relationship between contact angle and heat flux. Surface wettability affects the CHF substantially. The CHF for a hydrophilic ($\sim 0^\circ$) surface is several times higher of a hydrophobic ($\sim 127^\circ$) surface.
- As the pitch is increased, the heat flux also increases. For the lowest pitch (21.7 Å), the maximum CHF was $\sim 1.01 \times 10^8$ W/m². The largest overall flux occurred at the 106.6 Å pitch, with a maximum of 1.59×10^8 W/m².
- The 106.6 Å pitch case showed a 1–57% increase in CHF over the lower pitch cases.
- For pitches 65.1 Å and above, the temperature at which CHF occurs (and thus the degree of superheat) increases with increasing contact angle, and was also found to increase with pitch.

Lower than 65.1 Å, the combination of large contact angles and small pitches results in the liquid film eventually transitioning to a Cassie–Baxter state, which reduces overall heat transfer.

- This density and evaporation number data corroborate these findings, showing peaks that correspond to the onset of the CHF condition for each case.

Many future avenues can yet be explored regarding CHF based on contact angle and pitch. Further simulations should be performed exploring more super hydrophilic and hydrophobic interaction potentials to further illuminate the relationship between CHF and contact angle. The pitch of the nanostructures should also further be increased to determine its effect on peak CHF, as well as the temperature at which CHF occurs although computational cost increases with pitch. Different materials should also be simulated, that is, water as the working liquid and graphene, silicon, platinum, etc. as a substrate material.

Funding

This material is based upon the work supported by the National Science Foundation under Grant Nos. CMMI-1200557 and ECCS-1505706.

ORCID

Zhixiong Guo  <http://orcid.org/0000-0003-0481-2738>

References

- [1] D. G. Cahill, K. Goodson, and A. Majumdar, “Thermometry and thermal transport in micro/nanoscale solid-state devices and structures,” *J. Heat Transfer*, vol. 124, pp. 223–241, 2002. DOI: [10.1115/1.1454111](https://doi.org/10.1115/1.1454111).
- [2] G. Chen, *Nanoscale Energy Transport and Conversion*. Oxford, UK: Oxford University Press, 2005.
- [3] Z. Wu and B. Sundén, “On further enhancement of single-phase and flow boiling heat transfer in micro/minichannels,” *Renewable Sustainable Energy Rev.*, vol. 40, pp. 11–27, 2014. DOI: [10.1016/j.rser.2014.07.171](https://doi.org/10.1016/j.rser.2014.07.171).
- [4] C. H. Amon, S. C. Yao, C. F. Wu, and C. C. Hsieh, “Microelectromechanical system-based evaporative thermal management of high heat flux electronics,” *J. Heat Transfer*, 127, pp. 66–75, 2005. DOI: [10.1115/1.1839586](https://doi.org/10.1115/1.1839586).
- [5] C. Li, Z. Wang, P. Wang, Y. Peles, N. Koratkar, and G. P. Peterson, “Nanostructured copper interfaces for enhanced boiling,” *Small*, vol. 4, pp. 1084–1088, 2008. DOI: [10.1002/smll.200700991](https://doi.org/10.1002/smll.200700991).
- [6] T. Hendricks, S. Krishnan, C. Choi, C. H. Chang, and B. Paul, “Enhancement of pool boiling heat transfer using nanostructured surfaces on aluminum and copper,” *Int. J. Heat Mass Transfer*, vol. 53, pp. 3357–3365, 2010. DOI: [10.1016/j.ijheatmasstransfer.2010.02.025](https://doi.org/10.1016/j.ijheatmasstransfer.2010.02.025).
- [7] A. Kalani and S. G. Kandlikar, “Enhanced pool boiling with ethanol at subatmospheric pressures for electronics cooling,” *J. Heat Transfer*, vol. 135, p. 111002, 2013. DOI: [10.1115/1.4024595](https://doi.org/10.1115/1.4024595).
- [8] H. S. Ahn, V. Sathyamurthi, and D. Banerjee, “Pool boiling experiments on a nano-structured surface,” *IEEE Trans. Compon. Packag. Technol.*, vol. 32, pp. 156–165, 2009. DOI: [10.1109/tcapt.2009.2013980](https://doi.org/10.1109/tcapt.2009.2013980).
- [9] W. Wang, S. Huang, and X. Luo, “MD simulation on nano-scale heat transfer mechanism of sub-cooled boiling on nano-structured surface,” *Int. J. Heat Mass Transfer*, vol. 100, pp. 276–286, 2016. DOI: [10.1016/j.ijheatmasstransfer.2016.04.018](https://doi.org/10.1016/j.ijheatmasstransfer.2016.04.018).
- [10] D. Cooke and S. G. Kandlikar, “Pool boiling heat transfer and bubble dynamics over plain and enhanced microchannels,” *J. Heat Transfer*, vol. 133, p. 052902, 2011. DOI: [10.1115/1.4003046](https://doi.org/10.1115/1.4003046).
- [11] R. Mandel, A. Shooshtari, and M. Ohadi, “Thin-film evaporation on microgrooved heatsinks,” *Numer. Heat Transfer, Part A*, vol. 71, pp. 111–127, 2017. DOI: [10.1080/10407782.2016.1257300](https://doi.org/10.1080/10407782.2016.1257300).
- [12] S. M. You, J. H. Kim, and K. H. Kim, “Effect of nanoparticles on critical heat flux of water in pool boiling heat transfer,” *Appl. Phys. Lett.*, vol. 83, pp. 3374–3376, 2003.
- [13] H. S. Ahn and M. H. Kim, “A review on critical heat flux enhancement with nanofluids and surface modification,” *J. Heat Transfer*, vol. 134, p. 024001, 2012. DOI: [10.1115/1.4005065](https://doi.org/10.1115/1.4005065).
- [14] T. K. Tullius and Y. Bayazitoglu, “Analysis of a hybrid nanofluid exposed to radiation,” *Numer. Heat Transfer B*, vol. 69, pp. 271–286, 2016. DOI: [10.1080/10407790.2015.1104210](https://doi.org/10.1080/10407790.2015.1104210).
- [15] J. M. Wu and J. Zhao, “A review of nanofluid heat transfer and critical heat flux enhancement – research gap to engineering application,” *Prog. Nucl. Energy*, vol. 66, pp. 13–24, 2013. DOI: [10.1016/j.pnucene.2013.03.009](https://doi.org/10.1016/j.pnucene.2013.03.009).
- [16] D. Wen, G. Lin, S. Vafaei, and K. Zhang, “Review of nanofluids for heat transfer applications,” *Particuology*, vol. 7, pp. 141–150, 2009. DOI: [10.1016/j.partic.2009.01.007](https://doi.org/10.1016/j.partic.2009.01.007).

- [17] A. R. Betz, J. Xu, H. Qiu, and D. Attinger, "Do surfaces with mixed hydrophilic and hydrophobic areas enhance pool boiling," *Appl. Phys. Lett.*, vol. 97, p. 141909, 2010. DOI: [10.1063/1.3485057](https://doi.org/10.1063/1.3485057).
- [18] H. Jo, H. S. Ahn, S. Kang, and M. H. Kim, "A study of nucleate boiling heat transfer on hydrophilic, hydrophobic and heterogeneous wetting surfaces," *Int. J. Heat Mass Transfer*, vol. 54, pp. 5643–5652, 2011. DOI: [10.1016/j.ijheatmasstransfer.2011.06.001](https://doi.org/10.1016/j.ijheatmasstransfer.2011.06.001).
- [19] H. Ahn and G. Son, "Numerical simulation of liquid film evaporation in circular and square microcavities," *Numer. Heat Transfer A*, vol. 67, pp. 934–951, 2015. DOI: [10.1080/10407782.2014.949153](https://doi.org/10.1080/10407782.2014.949153).
- [20] R. F. Gaertner, "Photographic study of nucleate pool boiling on a horizontal surface," *J. Heat Transfer*, vol. 87, pp. 17–29, 1965. DOI: [10.1115/1.3689038](https://doi.org/10.1115/1.3689038).
- [21] H. S. Ahn, H. J. Jo, S. H. Kang, and M. H. Kim, "Effect of liquid spreading due to nano/microstructures on the critical heat flux during pool boiling," *Appl. Phys. Lett.*, vol. 98, p. 071908, 2011. DOI: [10.1063/1.3555430](https://doi.org/10.1063/1.3555430).
- [22] S. G. Kandlikar, "A theoretical model to predict pool boiling CHF incorporating effects of contact angle and orientation," *J. Heat Transfer*, vol. 123, pp. 1071–1079, 2001. DOI: [10.1115/1.1409265](https://doi.org/10.1115/1.1409265).
- [23] K. H. Chu, R. Enright, and E. N. Wang, "Structured surfaces for enhanced pool boiling heat transfer," *Appl. Phys. Lett.*, vol. 100, p. 241603, 2012. DOI: [10.1063/1.4724190](https://doi.org/10.1063/1.4724190).
- [24] Y. Zou, J. Cai, X. L. Huai, F. Xin, and Z. Guo, "Molecular dynamics simulation of heat conduction in Si nano-films induced by ultrafast laser heating," *Thin Solid Films*, vol. 558, pp. 455–461, 2014. DOI: [10.1016/j.tsf.2014.02.075](https://doi.org/10.1016/j.tsf.2014.02.075).
- [25] C. Y. Ji and Y. Y. Yan, "A molecular dynamics simulation of liquid-vapour-solid system near triple-phase contact line of flow boiling in a microchannel," *Appl. Therm. Eng.*, vol. 28, pp. 195–202, 2008. DOI: [10.1016/j.applthermaleng.2007.03.029](https://doi.org/10.1016/j.applthermaleng.2007.03.029).
- [26] B. Shi and V. K. Dhir, "Molecular dynamics simulation of the contact angle of liquids on solid surfaces," *J. Chem. Phys.*, vol. 130, p. 034705, 2009. DOI: [10.1063/1.3055600](https://doi.org/10.1063/1.3055600).
- [27] A. Hens, R. Agarwal, and G. Biswas, "Nanoscale study of boiling and evaporation in a liquid Ar film on a Pt heater using molecular dynamics simulation," *Int. J. Heat Mass Transfer*, vol. 71, pp. 303–312, 2014. DOI: [10.1016/j.ijheatmasstransfer.2013.12.032](https://doi.org/10.1016/j.ijheatmasstransfer.2013.12.032).
- [28] A. K. M. M. Morshed, T. C. Paul, and J. A. Khan, "Effect of nanostructures on evaporation and explosive boiling of thin liquid films: a molecular dynamics study," *Appl. Phys. A*, vol. 105, pp. 445–451, 2011. DOI: [10.1007/s00339-011-6577-8](https://doi.org/10.1007/s00339-011-6577-8).
- [29] H. R. Seyf and Y. Zhang, "Molecular dynamics simulation of normal and explosive boiling on nanostructured surface," *J. Heat Transfer*, vol. 135, p. 121503, 2013. DOI: [10.1115/1.4024668](https://doi.org/10.1115/1.4024668).
- [30] T. Fu, Y. Mao, Y. Tang, Y. Zhang, and W. Yuan, "Effect of nanostructure on rapid boiling of water on a hot copper plate: a molecular dynamics study," *Heat Mass Transfer*, vol. 51, pp. 1–10, 2015. DOI: [10.1007/s00231-015-1668-2](https://doi.org/10.1007/s00231-015-1668-2).
- [31] R. Diaz and Z. Guo, "A molecular dynamics study of phobic/philic nano-patterning on pool boiling heat transfer," *Heat Mass Transfer*, vol. 53, pp. 1061–1071, 2017. DOI: [10.1007/s00231-016-1878-2](https://doi.org/10.1007/s00231-016-1878-2).
- [32] S. Maruyama and T. Kimura, "A study on thermal resistance over a solid-liquid interface by the molecular dynamics method," *Therm. Sci. Eng.*, vol. 7, pp. 63–68, 1999. DOI: [10.1016/j.ijthermalsci.2007.01.009](https://doi.org/10.1016/j.ijthermalsci.2007.01.009).
- [33] Y. Mao and Y. Zhang, "Molecular dynamics simulation on rapid boiling of water on a hot copper plate," *Appl. Therm. Eng.*, vol. 62, pp. 607–612, 2014. DOI: [10.1016/j.applthermaleng.2013.10.032](https://doi.org/10.1016/j.applthermaleng.2013.10.032).
- [34] B. Dünweg and W. Paul, "Brownian dynamics simulations without Gaussian random numbers," *Int. J. Modern Phys. C*, vol. 2, pp. 817–827, 1991. DOI: [10.1142/s0129183191001037](https://doi.org/10.1142/s0129183191001037).
- [35] M. Isaiev, S. Burian, L. Bulavin, M. Gradeck, F. Lemoine, and K. Termentzidis, "Efficient tuning of potential parameters for liquid–solid interactions," *Mol. Simul.*, vol. 42, pp. 910–915, 2016. DOI: [10.1080/08927022.2015.1105372](https://doi.org/10.1080/08927022.2015.1105372).
- [36] S. Plimpton, "Fast parallel algorithms for short-range molecular-dynamics," *J. Comput. Phys.*, vol. 117, pp. 1–19, 1995. DOI: [10.1006/jcph.1995.1039](https://doi.org/10.1006/jcph.1995.1039).
- [37] W. Humphrey, A. Dalke, and K. Schulten, "VMD – visual molecular dynamics," *J. Mol. Graphics*, vol. 14, pp. 33–38. DOI: [10.1016/0263-7855\(96\)00018-5](https://doi.org/10.1016/0263-7855(96)00018-5).
- [38] R. Gilgen, R. Kleinrahm, and W. Wagner, "Measurement and correlation of the (pressure, density, temperature) relation of argon II. Saturated-liquid and saturated-vapour densities and vapour pressures along the entire coexistence curve," *J. Chem. Thermodyn.*, vol. 26, pp. 399–413, 1994. DOI: [10.1006/jcht.1994.1049](https://doi.org/10.1006/jcht.1994.1049).
- [39] M. Srivastava, "Image processing and analysis of vapor bubbles nucleated in thin liquid film boiling," Masters thesis, North Carolina State University, Raleigh, NC, 2015.
- [40] S. C. Maroo and J. N. Chung, "Molecular dynamic simulation of platinum heater and associated nano-scale liquid argon film evaporation and colloidal adsorption characteristics," *J. Colloid Interface Sci.*, vol. 328, pp. 134–146, 2008. DOI: [10.1016/j.jcis.2008.09.018](https://doi.org/10.1016/j.jcis.2008.09.018).
- [41] W. R. Gamble and J. H. Lienhard, "An upper bound for the critical boiling heat flux," *J. Heat Transfer*, vol. 111, pp. 815–818, 1989. DOI: [10.1115/1.3250759](https://doi.org/10.1115/1.3250759).
- [42] C. C. Hsu and P. H. Chen, "Surface wettability effects on critical heat flux of boiling heat transfer using nanoparticle coatings," *Int. J. Heat Mass Transfer*, vol. 55, pp. 3713–3719, 2012. DOI: [10.1016/j.ijheatmasstransfer.2012.03.003](https://doi.org/10.1016/j.ijheatmasstransfer.2012.03.003).
- [43] N. Khan, D. Pinjala, and K. C. Toh, "Pool boiling heat transfer enhancement by surface modification/micro-structures for electronics cooling: a review," presented at the Proceedings of 6th Electronics Packaging Technology Conference, pp. 273–280, Singapore, Singapore, 2004.